HOKKAIDO UNIVERSITY

Title	Modality of tumor endothelial VEGFR2 silencing-mediated improvement in intratumoral distribution of lipid nanoparticles
Author(s)	Yamamoto, Shoshiro; Kato, Akari; Sakurai, Yu; Hada, Tomoya; Harashima, Hideyoshi
Citation	Journal of Controlled Release, 251, 1-10 https://doi.org/10.1016/j.jconrel.2017.02.010
Issue Date	2017-04-10
Doc URL	http://hdl.handle.net/2115/68754
Rights	c2017, Elsevier. This manuscript version is made available under the CC-BY-NC-ND 4.0 license http://creativecommons.org/licenses/by-nc-nd/4.0/
Rights(URL)	http://creativecommons.org/licenses/by-nc-nd/4.0/
Type	article (author version)
File Information	manuscript.pdf

Title

Original article

Modality of tumor endothelial VEGFR2 silencing-mediated improvement in intratumoral distribution of lipid nanoparticles.

Shoshiro Yamamoto[§], Akari Kato[§], Yu Sakurai[§], Tomoya Hada, Hideyoshi Harashima*

Faculty of Pharmaceutical Sciences, Hokkaido University

[§] These three authors equally contributed to this manuscript

*Corresponding author

Correspondence should be addressed to Hideyoshi Harashima (harasima@pharm.hokudai.ac.jp)

Kita-12, Nishi-6, Kita-ku, Sapporo 060-0812, Japan.

E-mail: harasima@pharm.hokudai.ac.jp

TEL: +81-11-706-3919

FAX: +81-11-706-4879

Abstract

The vascular endothelial growth factor (VEGF)-mediated enhancement in vascular permeability is considered to be a major factor in tumor-targeting delivery via the enhanced permeability and retention (EPR) effect. We previously reported that the silencing of the endothelial VEGF receptor (VEGFR2) by a liposomal siRNA system (RGD-MEND) resulted in an enhanced intratumoral distribution of polyethylene glycol (PEG)-modified liposomes (LPs) in a renal cell carcinoma, a type of hypervascularized cancer, although the inhibition of VEGF signaling would be expected to decrease the permeability of the tumor vasculature. We herein report that the enhancement in the intratumoral distribution of LPs by VEGFR2 inhibition was dependent on the vascular type of the tumor (stroma vessel type;SV and tumor vessel type;TV). In the case of TV-type tumors (renal cell carcinoma and hepatocellular carcinoma), inhibiting VEGFR2 improved intratumoral distribution, while no effect was found in the case of SV-type tumors (colorectal cancer). Moreover, through a comparison of the intratumoral distribution of LPs with a variety of physical properties (100 nm vs 400 nm, neutral vs negative vs positive), VEGFR2 inhibition was found to alter the tumor microenvironment, including heparan sulfate proteoglycans (HSPGs). In addition, the results regarding the effect of the size of nanoparticles indicated that VEGFR2 inhibition improved the penetration of nanoparticles through the vessel wall, but not via permeability, suggesting the involvement of an unknown mechanism. Our findings suggest that a combination of anti-angiogenic

therapy and delivery via the EPR effect would be useful in certain cases, and that altering the tumor microenvironment by VEGFR2 blockade has a drastic effect on the intratumoral distribution of nanoparticles.

Introduction

The enhanced permeability and retention (EPR) effect, a major strategy for delivering macromolecules to tumor tissue, is characterized by "1) hypervasculature, 2) enhanced vaclular permeability as elicited by a factor, 3) negligible recovery of macromolecules via the blood vessels and 4) negligible recovery from the lymphatic system", as reported in the first study by Maeda dealing with the EPR effect [1]. Since this phenomenon was reported, a number of nano drug delivery systems (DDSs) based on the EPR effect have been developed [2]. Enhanced vascular permeability, which is driven by the vascular endothelial growth factor (VEGF) produced by various cells in tumor tissue, such as cancer cells, macrophages [3], fibroblasts [4], is considered to be a dominant factor in EPR effect-based delivery [5]. Actually, several enhancers of permeability, including VEGF itself, nitric oxide (NO) and bradykinin, have been reported to improve the therapeutic efficacy of EPR effect-based nanoparticles [6]. Thus, the immature, permeable vasculature in the tumor tissue is believed to mainly contribute to the extravasation of nanoparticles from the tumor vasculature to the extracellular space.

In contrast, we recently reported that the siRNA-mediated silencing of endothelial VEGF receptor 2 (VEGFR2) induced the maturation of the tumor vasculature and an unexpected elevation in tumor accumulation and the penetration of nanoparticles in a renal cell carcinoma (RCC) model of hypervascularized cancer [7]. These results were inconsistent with previously reported findings in

which permeability enhancers were reported to improve EPR effect-based delivery. We focused on remodeling the extracellular matrix (ECM) via VEGFR2 inhibition because the degradation of collagen and hyaluronic acid to low molecular weight compounds by enzymes also enhanced the EPR-based delivery of nanoparticles [8-10]. As a result, we found that VEGFR2 inhibition via siRNA delivery increased the numbers of infiltrating M1 type macrophages, and subsequently collagen degradation by matrix metalloproteinases (MMPs) produced from the increased numbers of macrophages, thus leading to an improved EPR effect-based delivery of nanoparticles in hypervascularized RCC. This discovery suggests that permeability is not the only determinant factor of the efficacy of EPR effect-based delivery. In other words, it would be wise to take into account the entire tumor microenvironment, including the number of cancer cells, other cell populations (macrophages, fibroblast etc.), ECMs, blood flow, to achieve the maximum outcome in the case of nanoparticle-based delivery. For purposes of this study, we defined the term "tumor accumulation" as the number of nanoparticles that flowed in the effective bloodstream, and subsequently penetrated tissue via the vessel wall (**Figure S1**). This was distinguished from the term "intratumoral distribution", which is defined as the extent of nanoparticles that diffused from the vasculature against the steric hindrance from cells and ECMs (**Figure S1**).

The use of anti-angiogenic therapy for cancer patients, such as anti-VEGF antibody Bevacizumab, anti-VEGFR2 antibody Ramucirumab, multi kinase inhibitors (Sunitinib, Sorafenib etc) and

inhibitors against mammalian target of rapamycin (mTOR) [11, 12] continues to expand.

Considering this present situation regarding anti-cancer treatment, the beneficial use of a

combination of antiangiogenic therapy and nanoparticles should be attempted in future clinical trials.

However, according to our traditional understanding of the EPR effect, anti-angiogenic therapy

would be expected to reduce therapeutic outcomes by nanoparticles because VEGF inhibition

reduces the permeability of the tumor vasculature [13, 14]. Concerning low molecular weight

compounds, anti-angiogenic therapy enhances the efficacy of therapeutics. For example, Irinotecan,

Fluorouracil and Leucovorin with Bevacizumab were found to be superior to that without

Bevacizumab in overall survival rate in cases of untreated metastatic colorectal cancer (CRC)

patients [15]. This improvement by inhibiting VEGF signaling in the therapeutic effects of low

molecular weight compounds can be attributed to a recovery of blood flow, the inhibition of leakage

in outer areas of the tumor tissue via lowered permeability and a decrease in interstitial fluid pressure

(IFP) [16]. On the other hand, the literature on relationships between anti-VEGF therapy and EPR

effect based delivery is sparse. In a human lung cancer model, VEGFR and platelet-derived growth

factor (PDGF) R inhibitor Pazopanib failed to improve the delivery of doxorubicin-loaded liposomes

[17], while in case of murine colorectal cancer, SU5416, a VEGFR2 inhibitor formulated into an

emulsion, enhanced the penetration of polyethylene glycol (PEG)-liposomes [18]. In another study,

Chauhan *et al.* reported that the improvement in the delivery of nanoparticles via VEGFR2

inhibition by the antibody DC101 was dependent on the size of nanoparticles by comparing the effect with Abraxane (12 nm) and Doxil (100 nm) [19]. No improvement was found for the intratumoral distribution of large size nanoparticles (100 nm) by VEGFR2 inhibition, while that for smaller sized nanoparticles (12 nm) was. Taken together, the effect of VEGF inhibition on the intratumoral delivery of nanoparticles remains a controversial subject, suggesting that its precise effect should be clarified for continued progress in the area of EPR effect-based delivery.

The objective of this study was to elucidate the precise mechanism responsible for the intratumoral distribution of nanoparticles that occur under conditions of VEGF inhibition conditions by using different types of nanoparticles and cancer cells. In this study, we prepared clusters of cancer cells based on spatial correlation of cancer cells and stroma including vasculature, as described in a previous report [20], leading to the producing stromal vessel type (SV) and tumor vessel type (TV) clusters. This clustering was first proposed in a study by Smith *et al* [20]. They classified various cancer types according to tumor stroma architecture of clinical tumor specimens; namely, vessels that were distributed around the tumor cells (TV) and vessels that were associated with stromal cells (SV). TV-type clusters were sensitive to anti-VEGF therapy while SV-type clusters did not respond to anti-angiogenic treatment. Therefore, they concluded that this structural phenotype determined the extent of response to anti-VEGF therapy. We hypothesized that these vasculature phenotypes also determined the effect of VEGFR2 inhibition on the distribution of

nanoparticles in the tumor tissue. In addition, to determine the optimized carrier and obtain further information on the effect of VEGF blockade, alterations in the intratumoral distribution of various types of liposomes (LPs) (neutral, anionic, cationic; small, large) were monitored.

To specifically silence endothelial VEGFR2 expression, we used a cyclic RGD peptide-modified liposomal siRNA system. We previously developed a system for delivering liposomal nucleic acids, a multi functional envelope-type nano device (MEND) [21-23]. The lipid envelope of the RGD-MEND consists of a pH-sensitive cationic lipid YSK05. YSK05 exhibits fusogenic properties at an acidic pH (<5.5) [24], which allows the RGD-MEND to escape from endosomes after being internalized. On the other hand, because YSK05 is neutral at physiological pH 7.4, a YSK05-containing MEND (YSK-MEND) would have a high biocompatibility. These characteristic properties of the YSK-MEND enabled us to inhibit mRNA expression, even in *in vivo* situations, such as the murine liver [25-28], a humanized chimeric liver infected with human hepatitis virus B and C [29, 30], liver sinusoidal endothelial cells [31], brain endothelial cells [32], peritoneal macrophages [33] and cancer cells [34, 35]. For tumor endothelial cell (TEC)-targeting, we modified the YSK-MEND with a cyclic RGD peptide (RGD-MEND), which is known to be a ligand against the $\alpha_V\beta_3$ integrin heterodimer, which is highly expressed in TECs and some types of cancer cells [36]. We previously reported that the RGD-MEND had the ability to suppress mRNA and protein expression specifically in TECs (ED50: 0.75 mg siRNA/kg) [37, 38].

In this manuscript, we report on an investigation of the effect of VEGFR2 inhibition on altering the intratumoral distribution of LPs and a tumor microenvironment with a clustered-vessel type cancer model by the RGD-MEND. We infer from these results that clustering cell types with regard to a relative position between tumor vessels and stroma might pose a difference in the response to altering tumor microenvironment therapy, including anti-angiogenic therapy.

2. Materials and Methods

2.1 Materials

Phosphate buffered saline without Ca^{2+} or Mg^{2+} (PBS (−)) was purchased from Wako Pure Chemical Industries (Osaka, Japan). Cholesteryl 3-N-(dimethylaminoethyl)carbamate hydrochloride (DC-chol) was purchased from AVANTI Polar Lipids (Alabaster, AL, USA) Distearoyl-*sn*-glycerophosphocholine (DSPC), polyethyleneglycol2000 (PEG) – distearoyl-*sn*-glycerophosphoethanolamine (PEG-DSPE), PEG-dimyristoylglycerol (PEG-DMG) and PEG-distearoylglycerol (PEG-DSG) were obtained from the NOF CORPORATION (Tokyo Japan). Cholesterol (chol), cholesterol hemisuccinate (CHEMS), TRI Reagent, Hoechst33342, RPMI-1640 and DMEM were purchased from Sigma-Aldrich (St. Louis, MO, USA). 1,1'-dioctadecyl-3,3,3',3'-tetramethylindocarbocyanine perchlorate (DiI) and 1,1'-dioctadecyl-3,3,3',3'- tetramethylindodicarbocyanine (DiD) were obtained from PromoKine (Heidelberg, Germany). [3H]-cholesteryl hexadecyl ether (CHE), Soluene-350 and Hionic-Fluor were purchased from PerkinElmer (Waltham, MA, USA). FITC-labeled isolectin B4 (GSIB4) was obtained from Vector Laboratories (Burlingame, CA, USA) the High-Capacity RNA-to-cDNA kit and Alexa647-labled GSIB4 were purchased from Thermo Fisher Scientific (Waltham, MA, USA). YSK05 was synthesized as previously described [24]. Primers were purchased from Sigma-Aldrich Japan (Ishikari, Japan), and all of the primer sets are listed in Supplemental Table 1. Anti-mouse

CD16/32 IgG (101302), PE anti-human HLA-A,B,C antibody (311406) and anti-mouse VEGFR2 rat

IgG (136402) were obtained from BioLegend (San Diego, CA, USA). Anti-mouse collagen Type 1,

α1 (COL1A1) rabbit polyclonal antibody was purchased from NOVUS Biologicals (Minneapolis,

MN, USA). All of siRNAs were synthesized at Hokkaido System Science (Sapporo, Japan), and

were listed in Supplemental Table 2. Cyclic RGD peptide was purchased from Peptides international

(Louisville, KY, USA). OS-RC-2 (human renal cell carcinoma, RCC), Huh-7 (human hepatocellular

carcinoma, HCC) and HCT116 (human colorectal cancer, CRC) were purchased from the ATCC.

2.2 Liposomes preparation

After mixing, 2000 nmol of DSPC and 2000 nmol of chol in a glass tube, the solvent was then

evaporated under a stream of nitrogen to produce a lipid thin layer. After warming 500 μL of PBS

(−) to 60°C, it was added to the lipid thin layer, followed by incubation at 600 rpm, 60°C for 30 min

for hydration. The suspension was then sonicated for 10 sec in a bath-type sonicator. Next, 500 μL of

pre-warmed PBS (−) was added to the suspension again and mixed with a vortex mixer for a few

seconds. The resulting mixture was extruded through polycarbonate membranes with nominal pore

sizes of 400, 200 and 100 nm in descending order (Small), or 400 nm only (Large). To remove

small-sized LPs in the Large LP solution, the solution was centrifuged (15000 g, 10 min, room

temperature), and the pellet was collected. The LPs were characterized using a Zetasizer Nano ZS

instrument (Malvern Instruments Ltd, Malvern, UK).

2.3 PEG-MEND and RGD-MEND preparation

The methods used to prepare both MENDs have been described in detail in previously

published papers [7, 37, 39]. Briefly, 40 - 160 μg of siRNA solution in 200 μL of citrate buffer (2

mM, pH 4.0) was stepwise added to 400 μL of 90% tertiary butanol (t-BuOH/double distilled water

(DDW) v/v) containing YSK05 (1,500 nmol), cholesterol (1,500 nmol) and PEG-DMG (45 nmol,

1.5 mol% of total lipid) under mixing. The mixture was diluted with PBS (−), and then subjected to

ultrafiltration with Amicon Ultra-15 (MERCK MILLIPORE, Darmstadt, Germany) to remove

un-encapsulated siRNA and t-BuOH. The encapsulation efficiency and a recovery rate of siRNA was

determined RiboGreen assay [35, 37, 39]. Cyclic RGD was conjugated to PEG-DSPE with

N-hydroxysuccinimide (RGD-PEG-DSPE) to display RGD peptide on the surface of the MENDs, as

previously described [37, 39]. To modify MENDs with RGD-PEG-DSPE (RGD-MEND), MENDs

were mixed with 3 mol% of PEG-DSPE in 7.5% ethanol (EtOH) (v/v) solution (2 mM citrate buffer,

pH 5.5), and then EtOH in the mixture was removed by ultrafiltration with an Amicon Ultra-15. A

particle size distribution and zeta-potential were measured with Zetasizer Nano ZS. When MENDs

were fluorescent labeled, 0.5 mol% of DiI or DiD was added to the initial lipid solution. When

MENDs with prolonged circulation time was prepared to induce knockdown in cancer cells, not in

TECs, 1.5 mol% of PEG-DMG in the initial lipid solution was replaced with 3.0 mol% of PEG-DSG (PEG-MEND). Besides, RGD-PEG-DSPE modification was not performed in case of PEG-MEND.

2.4 Animal model

ICR mice (4-week-old, females) were purchased from Japan SLC (Shizuoka, Japan). Balb/cAJcl nu/nu (nude) mice were obtained from Japan CLEA (Shizuoka, Japan). CB17/Icr-Prkdcscid/CrlCrlj (C.B-17 SCID) mice (4-week-old, male) was purchased from CHARLES RIVER LABORATORIES JAPAN (Kanagawa, Japan). To prepare the cancer model, 1×10^6 cells/70 μL PBS (−) of OS-RC-2 or 5×10^6 cells/70 μL PBS (−) of HCT116 or 5×10^6 cells/70 μL PBS (−) of Huh-7 were inoculated into nude mice (for OS-RC-2 and HCT116) or C.B-17 SCID mice (for Huh-7) on the right flank. Animal experiments were performed when the tumor volume reached 100 mm^3. For inoculating cells, they were cultured in DMEM for Huh-7 and HCT116 or RPMI-1640 for OS-RC-2, both of which media were supplemented with 10% fetal bovine serum, 100 U/mL of penicillin, 100 mg/mL of streptomycin, in humidified 5% CO_2 atmosphere at 37°C. In all of animal experiments, tumor volume was used at 100 ~ 400 mm^3. The experimental protocols were approved by the Hokkaido University Animal Care Committee in accordance with the guidelines for the care and use of laboratory animals.

2.5 Pharmacokinetics analysis of liposomes

To evaluate blood-concentration profile, ICR mice were systemically administered with approximately 800 nmol of liposomes labeled with DiD. At the indicated times (typically 0.016, 0.16, 0.5, 1, 3, 6, 24 h), 12 μL of blood was collected from the tail vein, and rapidly mixed with 1% SDS. The fluorescent intensity of the mixture was measured with Infinite M200 (Tecan, Männedorf, Switzerland). Blood concentration was calculated by interpolating the standard curve from the mixture of known amount of DiD-labeled liposomes and un-treated mice blood. The calculated area under the curve (AUC) was determined by fitting the concentration curve to a 2-compartment model with multi software. In the case of Supplemental Figure 2, AUC was calculated by trapezoidal rule because positive liposomes could not be fitted to 2-compartment model.

To evaluate the accumulation of liposomes in tumor tissue, LPs were labeled with approximately 15,000,000 degradation per minutes (dpm) of [^{3}H]-CHE. Other procedures were the same as the usual protocol. Tumor tissue was recovered at 24 h after tumor-bearing mice were systematically injected with 3,000,000 dpm of liposomes. Tumor tissues were incubated in 2 mL of Soluene-350 at 55°C overnight, and the red pigment derived from red blood cells was then quenched by three additions of 100 μL of H_2O_2. Samples were kept at 4°C overnight after adding 10 mL of trimethyl benzene-type liquid scintillation cocktail Hionic-Fluor to attenuate non-specific chemiluminescence. The radioactivity of each sample was measured with LSC-6100 counter (Hitachi-Aloka Medical,

Tokyo, Japan).

2.6 Observation of intratumoral distribution of liposomes and MENDs

To avoid artificial results during the fixation of tumor sections, row sections (neither frozen nor fixed) were used for observation of the intratumoral distribution of liposomes and MENDs. Approximately, 500 nmol of DiD-labeled liposomes or MENDs were intravenously administered into tumor-bearing mice, and tumor was collected in PBS (−) after 24 h. The tumor tissues were then sliced at a 400 μm thickness, and the sliced sections were immersed in PBS (−) containing 10 μg/mL of FITC-labeled GSIB4 and 10 μg/mL of Hoechst33342 until being observed. Tumor sections were set on coverslips (1.7 mm thickness, Matsunami), and then observed with Nikon A1R (Tokyo, Japan). CFI Plan Fluor 10×, CFI Plan Apo Lambda 20× or CFI Plan Apo VC 60× water immersion objective lens were used for observation. To confirm that changes in intratumoral distribution via VEGFR2 inhibition occurred over the entire tumor tissue, we obtained whole images of tumor sections. Quantification of distribution area was performed by Fiji software. In the image analysis, a lower threshold was determined by using un-treated tumor sections.

2.7 Observation of protein expression with cryosection

Tumor tissues was collected, and then fixed by immersing them in 4% paraformaldehyde

overnight at 4°C. To remove water from the tissues, the fixed tissues were immersed twice in a 4%

sucrose phosphate buffer (pH 7.4; PB), 10% sucrose PB for 30 min, 15% sucrose for 30 min and

finally 20% sucrose PB overnight. The tissues were embedded in OCT compound (Sakura Finetek

Japan, Tokyo, Japan). The embedded tissues were sectioned at a 5-10 μm thickness with CM3050S

(Leica Microsystems, Nussloch, German), and the sections were placed on the MAS-coated

slideglass (Matsunami, Osaka, Japan). To prevent non-specific binding of the antibody, the sections

were kept in PBS (−) containing 1.5% bovine serum albumin and 0.05% sodium azide for 1 h, and

then washed with PBS (−). The dilution rate of first and second antibody was 200-fold. After a final

wash, 2 μg/mL of Hoechst33342 was added. After wash by PBS (−), cover slips (Matsunami, #1s)

were put on the section with a little amount of ProLong Gold (Thermo Fisher Scientific). After

fixing the cover slips with nail polish, they were kept at 4°C to permit the ProLong Gold solution to

solidify.

2.8 RNA isolation and qRT-PCR

After the tumor tissues were excised and minced by scissors, the minced tissues were

homogenized PreCellys (Bertin Technologies, Montigny-le-Bretonneux, France) with 1.4 mm

zirconium beads in 500 μL of TriReagent. Following procedures were done according to the

manufacturer's instructions. Then, 1.0 μg of total RNA was reverse transcribed with a High-Capacity

RNA-to-cDNA kit. The obtained cDNA was diluted, and then subjected to the quantitative reverse transcription – polymerase chain reaction (qRT-PCR). The expression level of mRNA was calculated by the ΔΔCt method. It was confirmed that the amplification efficiency of all primer sets exceeded 90%.

2.9 FACS analysis

To quantify the intratumoral distribution of the PEG-MEND, the fluorescent intensity derived from DiD-labeled MEND in each cell type was measured as previously described [7]. Briefly, the minced tumor tissue was digested in 10 mg/mL type II collagenase for 1 h at 37°C, and the resulting tissue was passed through a 100-μm cell strainer (BD Falcon, San Jose, CA, USA). Red blood cells in cell dispersions were lysed by 155 mM ammonium chloride after washing twice with Hank's balanced salt solution (HBSS). Then, 1×10^6 cells were mixed with anti-mouse CD16/32 rat IgG for blocking. To distinguish cancer cells from other cell populations, the cells were reacted with PE anti-human HLA-A,B,C antibody (311406). DiD fluorescence in HLA-A,B,C$^+$/propidium iodide$^-$ cells was measured with FACSCalibur (BD Falcon, San Jose, CA, USA).

2.10 Statistical analysis

Statistical analyses were performed by the two-tailed Student's t-test (two groups) or analysis of

variance (ANOVA) followed by SNK test. In this study, a p-value < 0.05 was regarded as a

statistically significant difference.

3. Results

3.1 Comparison of alterations in intratumoral distribution between small and large liposomes in

endothelial VEGFR2 inhibited RCC tumors

We first examined the difference in intratumoral distribution between small and large LPs under a

treatment with RGD-MENDs that had been pretreated with siRNA against VEGFR2 (siVR2 (+)). On

the other hand, no pre-injection of the RGD-MEND was regarded as siVR2 (−). As the area under

the curve (AUC) of therapeutics is known to be a dominant factor in the EPR effect-based delivery

of therapeutics [40], we attempted to prepare average diameter 105 nm (Small) and 381 nm (Large)

LPs with approximately the same AUC by altering the amount of PEG-lipid in the particle. The

characterization data for the Small and Large LPs are summarized in Supplemental Table 3. The

AUC of Small LPs with PEG2k-DSPE 2 mol% LPs was 362 % of the injected dose (%ID)/mL blood

while that of Large LPs with 7 mol% PEG2k-DSPE was 300 %ID/mL of blood (**Figure S2**).

Before the administration of fluorescent labeled LPs, siVR2 was systematically administered to

RCC-bearing mice via the tail vein 3 times at a dose of 3.0 mg/kg. Fluorescent labeled LPs were

injected at the same time as the 3rd injection of siVR2, and the intratumoral distribution of Small

and Large LPs was then examined. The intratumoral distribution of Small LPs was significantly

increased by the siVR2 treatment (**Figure 1A left, B**). To our surprise, the intratumoral distribution

of Large LPs was also markedly enhanced by the siVR2 injection (**Figure 1A right, B**). Concerning

accumulation, no significant difference was observed between the Small and Large LPs, although the

extent of accumulation was slightly increased (**Figure 1C**). The difference between the con focal

laser scanning microscopy (CLSM) study and the RI-based accumulation study can be attributed to

the strictly restricted diffusion of Large LP in the absence of siVR2. In the case of siVR2 (−), Large

LPs were closely retained around the vessels. This explains why the fluorescent intensity in each

pixel was saturated. On the other hand, the diffusion of Large LPs appeared to be expanded as the

result of the siVR2 treatment, which could result in the cancellation of the saturated fluorescent

intensity. In such a situation, if the level of accumulation remained unchanged, it would be likely

that the expected accumulation of LPs from the CLSM results did not reflect that actual amount of

accumulation.

Since the siVR2 injection led to the maturation of the tumor vasculature, the endothelial cell-cell

junction would be expected to become more tight. Under such conditions, Large LPs would not pass

through the vessel wall. To exclude the possibility that the siVR2 treatment caused an unexpected

loss of endothelial junction, we observed vascular endothelial cadherin (VEcad) expression, which

plays a key role in the endothelial junction and is regarded as a marker of vascular permeability

[41-43]. The level of VEcad expression was significantly elevated as the result of the siVR2

treatment, indicating that the endothelial cell-cell junction became more tight in comparison to

un-treated mice (**Figure 2A, B**). However, the localization of VEcad was also altered. After the

siVR2 treatment, VEcad was localized over all tissues, not on vessels. In the case of a Large LP,

CLSM images indicated an elevated amount of accumulation. However, since the siVR2 treatment

had no effect on the blood concentration of Large LPs (**Figure S3**), the red signals in Large LP in

CLSM images indicated the absence of LPs in the blood circulation. Accordingly, Large LPs appear

to penetrate tumor vessel through the mature vasculature somehow. Control siRNA encapsulated into

the RGD-MEND had a slight effect on increasing VEcad expression, but this effect was not

statistically significant. Judging from these results, not only would be the vascular permeability a

determinant factor for nanoparticles delivery.

Figure 1. The intratumoral distribution and accumulation of Small and Large LPs. A) The

effect of pre-siVR2 treatment on the intratumoral distribution of LPs. Green and red dots denote

vessels and LPs, respectively. Scale bars are 100 μm for magnified images, 1000 μm for whole

images. B) Quantitative data of magnified images in Figure 1A. Red pixels indicating LPs were

divided by green pixels indicating vessels. Student's t-test was performed between siVR2 (−) and (+).

*:p<0.05, * p<0.01 (n=6-8). C) Amounts of Small and Large LPs that accumulate in tumor tissue,

with or without siVR2 treatment. Radioactivity in tumor tissues was measured with liquid

scintillation counter 24 h after [³H]-CHE-labeled LPs were administered into OS-RC-2-bearing mice.
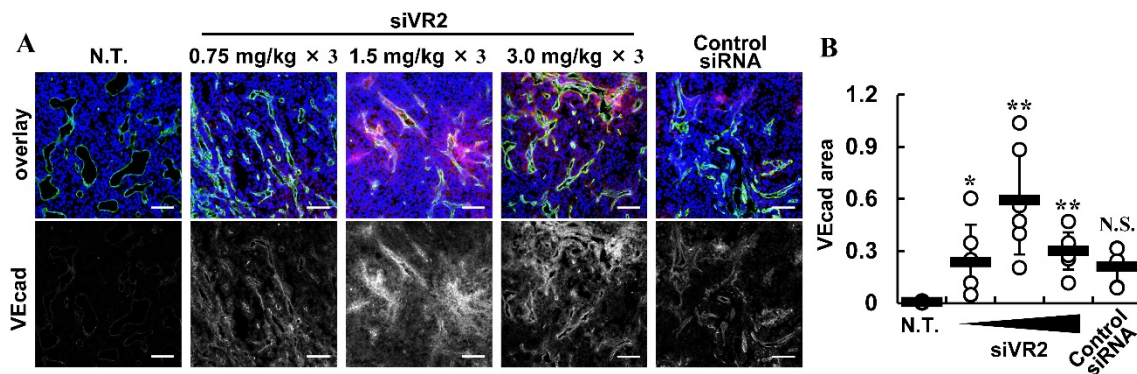
Data represent the mean ± standard deviation. (n=3)

Figure 2. VEcad expression as an indicator of the integrity of the tumor vasculature. A)

Representative images of VEcad expression. VEcad expression was investigated when siVR2 or

control siRNA encapsulated in the RGD-MEND were 3 times administered at doses of 0.75, 1.5 or

3.0 mg/kg. In the upper panels, blue, green and red dots indicate the nucleus, CD31 and VEcad,

respectively. In the lower panels, VEcad is shown in grayscale mode. B) Quantified data from A).

VEcad pixels were normalized to nucleus pixels because theoretically VEcad didn't exist in vascular

lumens. For statistical analysis, non repeated ANOVA was performed, followed by the Bonferroni

test (vs. non treatment (N.T.)). P>0.05 was regarded as not statistically significant difference. Scale

bars are 100 μm.

3.2 Comparison of altering intratumoral distribution among various surface charged liposomes in

endothelial VEGFR2 inhibited RCC tumor

We then examined the effect of surface charge of LPs. To change the surface charge of the Small

LP without drastic changing in lipid packing, structure and stability, we used cholesterol derivatives

instead of cholesterol; CHEMS for negatively charged Small LP ($Small_{neg}$) and DC-chol for

positively charged Small LP ($Small_{pos}$). The characterization of these Small LPs is summarized in

Supplemental Table 4. While the diameters of LPs were almost the same, the zeta-potential of these

LPs were prepared to function at pH 6.5, which was assumed to be tumor acidic conditions by the

Warburg effect [44]. The AUC values for these LPs were completely different (**Figure S4**). Above

all, the $Small_{pos}$ was present in low blood at relatively low concentrations early on, but then

recovered. This is because once a cationic LP accumulates in the lung, it is then gradually released

from the lung [45].

To allow us to readily compare the intratumoral distribution of LPs with different AUCs, the

injected fluorescence intensity was adjusted to be the same among three Small LPs, only in Figure

3A and 3B. The intratumoral distribution of Small and $Small_{neg}$ was improved (**Figure 3A, B**).

However, only the intratumoral distributed $Small_{pos}$ appeared to be localized on vessels in the

presence of siVR2 (+) (**Figure 3A ,B and Figure S5**), but not significant (**Figure 3C**). Tumor

accumulation of $Small_{pos}$ was significantly enhanced by the siVR2 treatment, whereas the elevation

of Small and Small_neg, while they were slightly increased, the increase was not significant (**Figure 3D**). Taken together, the mode of improvement in the intratumoral distribution of LPs was dependent on the charge of the nanoparticle.
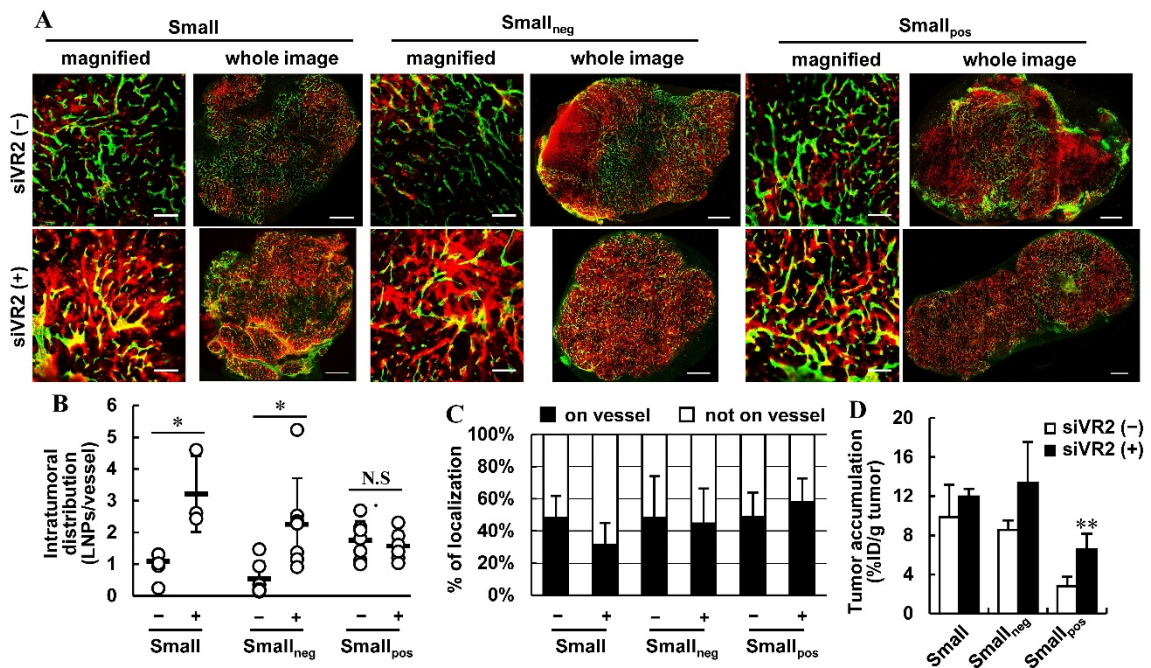

Figure 3. The intratumoral distribution and accumulation of neutral, negative and positive LPs. A) The effect of pre-siVR2 treatment on the intratumoral distribution of LPs. Green and red dots denote vessels and LPs, respectively. In this experiment, the dosage of each of the LPs was adjusted to shown the same AUC of fluorescence as the lowest Small_pos LP. Scale bars are 100 μm for magnified images, 1000 μm for whole images. B) Quantitative data of the magnified images in Figure 2A. Red pixels indicating LPs were divided by green pixels indicating vessels. The signs – and + mean that siVR2 (–) and siVR2 (+), respectively. The Student's t-test was performed between

siVR2 (−) and (+). *:p<0.05 (n=6-8). C) The change in localization of each LPs. White and black column mean LPs not on vessel and LPs co-localized on vessels, respectively. The signs – and + mean that siVR2 (–) and siVR2 (+), respectively. D) Accumulation amount of Small, $Small_{neg}$ and $Small_{pos}$ LPs with or without siVR2 treatment. Radioactivity in tumor tissues was measured by liquid scintillation counting 24 h after OS-RC-2-bearing mice were administered with $[^3H]$-CHE-labeled LPs. Data represent the mean ± standard deviation. (n=3)

3.3 Analysis of improvement mode in different tumor types

As mentioned above, we chose cancer cells according to clustering TV and SV; Huh-7 (human HCC) as TV and HCT116 (human CRC) as SV. We first observed the alteration of LPs in the intratumoral distribution by CLSM. As a result, in the case of Huh-7 model (TV-type), the intratumoral distribution of LPs was significantly improved, while that of HCT-116 (SV-type) was markedly reduced (**Figure 4A**). To quantitatively measure the intratumoral distribution of LPs, the extent of cellular uptake by either of the cells was determined by flow cytometry. Cellular uptake was improved in the case of Huh-7 model (**Figure 4B upper**). However, that for HCT-116 became worse (**Figure 4B lower**). We then examined the effect of the improvement in the intratumoral distribution by siVR2 on the pharmacological efficacy of liposomal siRNA (PEG-MEND), which could induce gene silencing in cancer cells [34]. As for TV-type tumor, the silencing of human cancer associated gene *polo*-like kinase 1 (PLK1) was significantly improved by siVR2 in human RCC OS-RC-2, whereas it was slightly, but not significantly, enhanced in the case of human HCC Huh-7. On the other hand, we were not able to assess the effect of siVR2 on the silencing effect of the PEG-MEND because it is very difficult to deliver siRNA to SV type tumors using 100 nm diameter PEG-MENDs (Figure S5). We therefore were not able to examine the effect of siVR2 in pharmacological effects in SV-type tumors. These results suggest that the siVR2 treatment improved the intratumoral distribution of LPs in TV-type HCC, but not SV-type CRC.
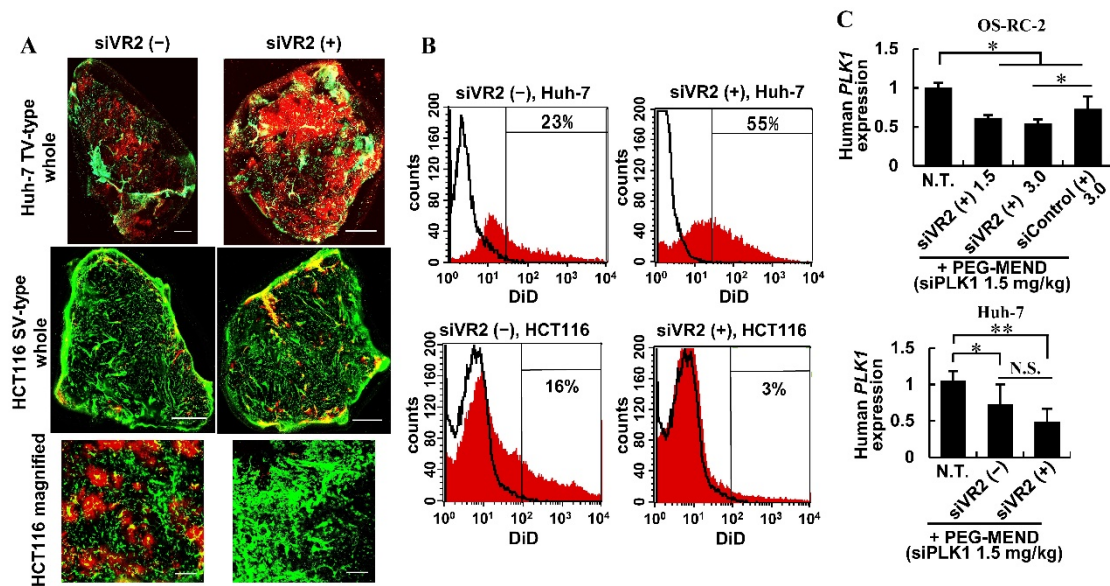
Figure 4. The intratumoral distribution of LPs in comparison with tumor vessel (TV)-type and stroma vessel (SV)-type tumors. A) The effect of a pre-siVR2 treatment on the intratumoral distribution of LPs. Green and red dots means vessels and LPs, respectively. Scale bars are 100 μm for magnified images, 1000 μm for whole images. B) Quantitative data of LPs taken up by cancer cells. Black solid line means fluorescent intensity from un-treated mice. Red filled histogram means the fluorescent intensity from mice treated from fluorescent labeled LPs. The value indicates the population of cell fraction in which LPs-derived fluorescence was detected. C) Pharmacological effect of siVR2 on the silencing effect of tumor-targeting liposomal siRNA (PEG-MEND). Human *PLK1* mRNA expression was measured by qRT-PCR 24 h after the injection of PEG-MEND. siVR2 (+) 1.5 and siVR2 (+) mean that RGD-MEND loaded with siRNA against VEGFR2 was injected 3 times at a dose of 1.5 or 3.0 mg/kg, respectively, before the injection of the PEG-MEND. siControl

(+) 3.0 means that siRNA against luciferase encapsulated in the RGD-MEND was administered 3

times at a dose of 3.0 mg/kg before the injection of the PEG-MEND. Upper and lower graphs means

the gene knockdown data in OS-RC-2 and Huh-7, respectively. Data represents mean ± standard

deviation. Statistical analyses were performed by non-repeated ANOVA, followed by SNK test.

(n=3-6)

To identify the factors responsible for this difference between TV-type and SV-type, we examined the maturation of the tumor vasculature and ECM remodeling. Alpha smooth muscle actin (αSMA) is generally regarded as an indicator of vascular maturation. In Huh-7, a siVR2 injection had no effect on the extent of vascular maturation (**Figure 5**). Likewise, αSMA was not increased in HCT116 (**Figure 5**). Thus, vascular maturation does not explain the difference in the mode of improvement in intratumoral distribution between TV-type Huh-7 and SV-type HCT116.

We examined the expression of collagen, a typical ECM component, because we previously reported that collagen degradation by macrophages that was induced as the result of an siVR2 injection enhanced the intratumoral distribution and accumulation of LPs [7]. Unlike the previous report, the amount of type I collagen 1α (COL1A1) was not changed by the siVR2 treatment in the case of Huh-7 (**Figure 6A right, B**). On the other hand, was COL1A1 markedly increased in the case of HCT116-bearing mice (**Figure 6A left**). In addition, the knockdown of VEGFR2 was observed in the both model (**Figure S6**). These results suggest that a change in intratumoral distribution does not explain the difference in VEGFR2 knockdown efficiency. Thus, ECMs, including COL1A1, affected the intratumoral distribution of EPR effect-based nanoparticles. Further, to elucidate how an increase of COL1A1 in HCT116 tumors could inhibit the intratumoral distribution of LPs, changes in the number of functional vessels were examined. Dense arrays of collagen molecules would be expected to compress a tumor vessel via solid stress. In a previous

report by Chauhan *et al.*, found that the amount of collagen I was inversely correlated to the proportion of perfused vessels [46]. Moreover, they discovered that the angiotensin II receptor blocker losartan suppressed the activity of cancer associated fibroblast (CAF), which is a major producer of collagen [47], via the inhibition of type 1 angiotensin II receptor. Losartan decreased the content of collagen I by suppressing CAF, and consequently increased the amount of perfused vessels. Thus, collagens not only restrict the diffusion of nanoparticles but also obstruct blood flow in tumor tissue. Based on this information, we determined the population of vessels with blood flow by comparing vessels that were stained by the intravenous injection of FITC-labeled GSIB4 prior to their collection and vessels (vessels with the blood flow) that were stained by immersing the collected tumor tissue in Alexa Fluor 647-labeled GSIB4 (all vessels). The findings indicate that functional vessels were decreased by the siVR2 treatment in HCT116 (**Figure S7**). Taken together, the reaction to the inhibition of VEGF signals was completely different between TV- and SV-type tumor tissues.
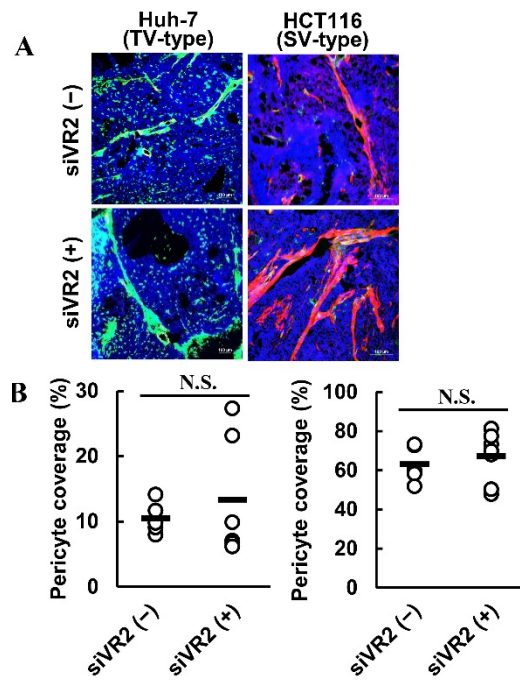
Figure 5. The change of COL1A1 expression by siVR2 treatment with tumor vessel (TV)-type and stroma vessel (SV)-type tumors. A) The effect of pre-siVR2 treatment on COL1A1 expression. Blue, green and red dots means nucleus, vessels and αSMA, respectively. Scale bars are 100 μm. B) Quantitative data of pericyte coverage. Statistical analysis was performed by Student's t-test. (n=5-6)
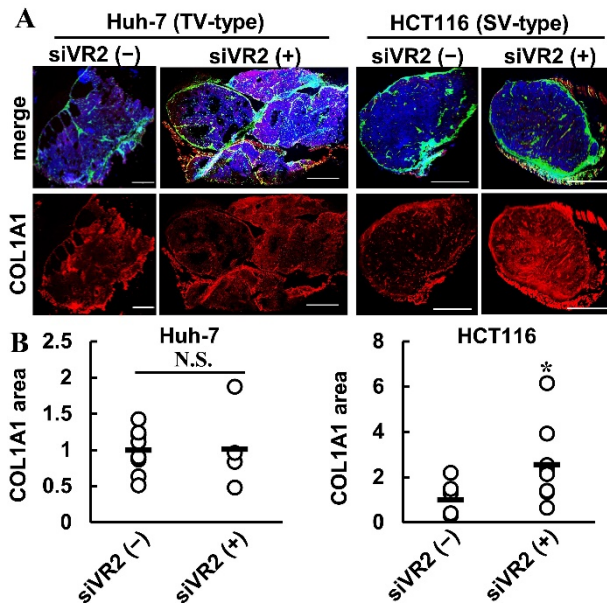
Figure 6. Alteration in type I collagen by siVR2 in comparison with tumor vessels (TV)-type and stroma vessels (SV)-type tumors. A) Whole images of COL1A1 in Huh-7 (TV-type) and HCT116 (SV-type) xenografts. COL1A1 in the tumor tissues with or without siVR2 pretreatment were observed. Blue, green and red dots indicate nucleus, vessels and COL1A1, respectively. Scale bars are 1000 μm.

Discussion

The findings reported herein show that the suppression of VEGF signaling in endothelial cells could enhance intratumoral distribution specifically in TV-type tumor, but not in SV-type tumors, which would include several implications.

Notably, siVR2 injection enhanced the intratumoral distribution of not only Small LPs but also Large LPs. VEGF acceleration played an important role in the abnormality of the tumor vasculature [48]. For example, the sizes of the intercellular gap and intracellular hole were identified to be 1.7 ± 0.1 μm 0.6 ± 0.1 μm in MCa-IV (murine breast cancer) model by transmittion electron microscopy (TEM) [49]. Generally, the size of the gap is in the range from 100 to 800 nm [50]. Nanoparticles pass through such pores in endothelial cells. An siVR2 treatment should led to the maturation of the tumor vasculature. Accordingly, the size of the intercellular gap and intracellular hole (fenestrae) would be reduced. Actually, our previous results revealed that the tumor vasculature matured as the result of a siVR2 treatment in the case of a TV-type RCC tumor model [7]. In this case, the levels of the endothelial cell junction protein VEcad were substantially increased as the result of the siVR2 treatment (**Figure 2**). Taken together, the improvement in the intratumoral distribution of Large LPs by the siVR2 treatment could not be explained by vascular permeability. Considering nanoparticles containing albumin-bound paclitaxel (Abraxane), which is known to be delivered to tumor tissue via transcytosis through a vessel wall [51]. Abraxane first binds to endothelial protein GP60, and is then

internalized by endothelial cells via caveolin-mediated endocytosis [52-54]. This may be the case in another nanoparticle delivery. Further study will be needed for the elucidation of the mode of penetration of nanoparticles when the tumor vasculature is mature.

The surface charge of LPs also affect the modality of the improvement of intratumoral distribution by siVR2. The intratumoral distribution of cationic LPs ($Small_{pos}$) deteriorated while that of neutral (Small) and anionic LPs ($Small_{neg}$) was enhanced as the result of the siVR2 treatment. Before the treatment, the intratumoral distribution of $Small_{pos}$ LPs was superior to Small and $Small_{neg}$. This may be because cationic nanoparticles were able to penetrate into the tumor tissue more deeply via transcytosis [55]. On the other hand, magnified images revealed that $Small_{neg}$ was localized on the vessel (**Figure 3**). This change can be attributed to the elevated levels of heparan sulfate proteoglycans (HSPGs) caused by siVR2 (**Figure S8**). As a result of measurements of HSPGs including Syndecans (*Sdn*) and Glypicans (*Gly*), *Sdc2*, *Gpc1* and *Gpc2* were elevated by the siVR2 treatment in dose-dependent manner. On the other hand, *Sdc1*, *Sdc4* and *Gpc3* were increased by control siRNA encapsulated in RGD-MEND. As VEGFR2 and HSPGs coordinately facilitate the development of angiogenesis [56], the inhibition of VEGFR2 by siVR2 altered the expression of some HSPGs. Likewise, a recent study showed that an anti-VEGF antibody treatment resulted in increased levels of glycosaminoglycans (GAGs) [57]. In addition, the cyclic RGD peptide itself had an inhibitory function by binding $\alpha_v\beta_3$ integrin [58]. Accordingly, siVR2 treatment deteriorated the

intratumoral distribution of Small$_{pos}$ LPs. In summary, tumor stroma containing ECMs and GAGs should be taking into consideration in assessing the intratumoral distribution of EPR effect-based nanoparticles.

The results of a comparison between TV and SV-type tumors implied that the architecture around the vasculature could be a dominant factor for EPR effect-based delivery. We currently hypothesize that TV-type tumors are hypervascularized and stroma-poor whereas SV-types are hypovascularized and stroma-rich, and that blood flow, vascular permeability and ECMs remodeling are closely related. Our results suggest that the response to siVR2 was completely different. In the case of the TV-type cluster, the siVR2 treatment led to the degradation of collagen molecules and consequently the intratumoral distribution of LPs. On the other hand, siVR2 significantly increased the level of collagen molecules and deteriorated the intratumoral distribution of LPs in the case of SV-type tumors. Sakai *et al.* reported that the co-inoculation of cancer cells and fibroblast growth factor (FGF)-2 significantly increased collagen expression and thus reduced the therapeutic efficacy of Abraxane in the case of stroma-rich human pancreatic cancer (PC) BxPC3 [58]. Taken together, ECMs might be more intimately involved in EPR effect-based delivery than vascular permeability.

The difference between TV- and SV-type on EPR effect-based delivery has been reported. Miano *et al.* clarified that lipid nanoparticles were taken up less by cancer cells in the case of SV-type tumors, since the abundant numbers of fibroblasts in the TV-type preferentially took up lipid

nanoparticles. Thus, it would be expected to be difficult to apply EPR effect-based delivery to SV-type cancer therapy. In spite of our efforts, we also failed to achieve gene silencing in SV-type tumors using a 100 nm diameter PEG-MEND (**Figure S5**). For this reason, it was not possible to evaluate the effect of siVR2 treatment on the pharmacological effect of nanoparticles in SV-type tumors. According to reference [20], SV-types include epithelial, adenocarcinoma (CRC, PC, lung cancer), which common malignant neoplasms. For this reason, a solution to improving therapeutic efficacy in those SV-type cancers should be very important. Inhibition of transforming growth factor (TGF)-β is one of solutions against this issue. A TGF-β inhibitor was reported to enhance the EPR effect-based delivery of 100 nm liposomes in BxPC-3 model [59]. Furthermore, the effect of tumor stroma on the intratumoral distribution of nanoparticles was diminished when the size of nanoparticles was reduced [60]. This implies that, if we could have used size-limited nanoparticles in siRNA delivery, it would have been possible to assess the effect of the siVR2 treatment on the gene silencing effect, even in SV-type tumors. However, recent studies revealed that small-sized lipid nanoparticles are unstable in the bloodstream [27, 61]. Therefore, methodology directed at altering tumor microenvironment to achieve optimal EPR effect-based delivery represent crucial issues in addition to development the small-sized stable nanoparticles in the bloodstream. In summary, further study will be needed for a complete understanding of the underlying mechanisms between the relationship between ECM/tumor stroma and nanoparticle delivery and the difference in ECM

remodeling by VEGF inhibition to be elucidated among cancer types.

Moreover, the manipulation of tumor models can have an effect on clinical tumor tissue. The results of a recent meta-analysis suggested that anti-cancer drugs formulated into liposomes are not statistically significant, and not a non-clinical model [62]. This paper suggested that the subcutaneous inoculation model did not reflect on the relevance of clinical tumor tissue. Actually, almost all xenografts exhibited the TV-type characteristic phenotype, even though clinical tumor tissues were the SV-type phenotype [20]. This is because the speed of growth of xenograft models and murine syngeneic graft models are higher than that for a clinical tumor. Specifically, the rapidly growing murine syngeneic model might be inappropriate for exploring EPR effect-based delivery. In addition, several studies have revealed that the structure of tumor vasculature differed as the tumor continued to grow [63, 64]. In these reports, when the size of the tumor tissue was small, the vasculature was not covered by pericytes. It is currently unclear which model was appropriate for an evaluation of EPR effect-based delivery. In the near future, a tumor model which is more similar to the clinical tumor tissue will be needed for continuing progress in nanoparticles-based delivery.

In addition to the above findings, the difference in ECM remodeling and the intratumoral distribution of LPs by the inhibition of VEGF signaling suggests that the EPR effect might be more complicated than expected. This would be the first study to reveal that the inhibition of VEGF signaling by nanoparticle delivery was completely different between TV- and SV-type tumors. Such

a difference in response against another treatment intended to alter the tumor microenvironment is possible. In future studies, we plan to establish a novel, unified concept for the delivery of tumor-targeting nanoparticles.

Conclusions

Although the inhibition of VEGF signaling suppressed EPR effect-based delivery, based on traditional understanding for the EPR effect, our results suggest that VEGFR2 inhibition by liposomal siRNA against VEGFR2 (siVR2) exerts the intratumoral accumulation and the distribution of nanoparticles in tumor vessel (TV)-type tumors including renal cell carcinoma and hepatocellular carcinoma. On the other hand, in the case of SV-type HCT116, siVR2 deteriorated the intratumoral distribution of particles via the increased extracellular matrixes (ECMs). These findings imply that cancer cell types, vascular structure and ECMs as well as vascular permeability when the EPR effect-based delivery is developed and designed, all have to be taken into consideration.
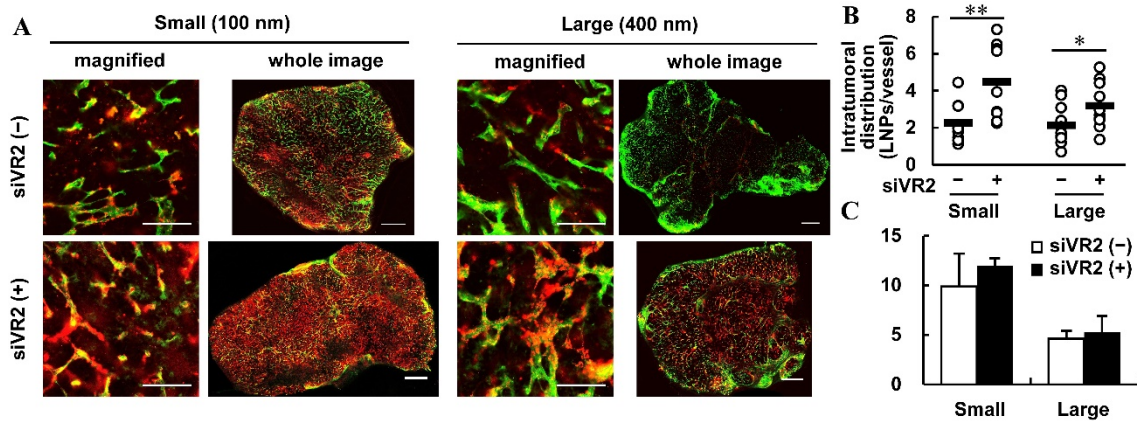
Acknowledgements

Figure legends

Figure 1. The intratumoral distribution and accumulation of Small and Large LPs. A) The effect of pre-siVR2 treatment on the intratumoral distribution of LPs. Green and red dots denote vessels and LPs, respectively. Scale bars are 100 μm for magnified images, 1000 μm for whole images. B) Quantitative data of magnified images in Figure 1A. Red pixels indicating LPs were divided by green pixels indicating vessels. Student's t-test was performed between siVR2 (−) and (+). *:p<0.05, * p<0.01 (n=6-8). C) Amounts of Small and Large LPs that accumulate in tumor tissue, with or without siVR2 treatment. Radioactivity in tumor tissues was measured with liquid scintillation counter 24 h after [3H]-CHE-labeled LPs were administered into OS-RC-2-bearing mice. Data represent the mean ± standard deviation. (n=3)
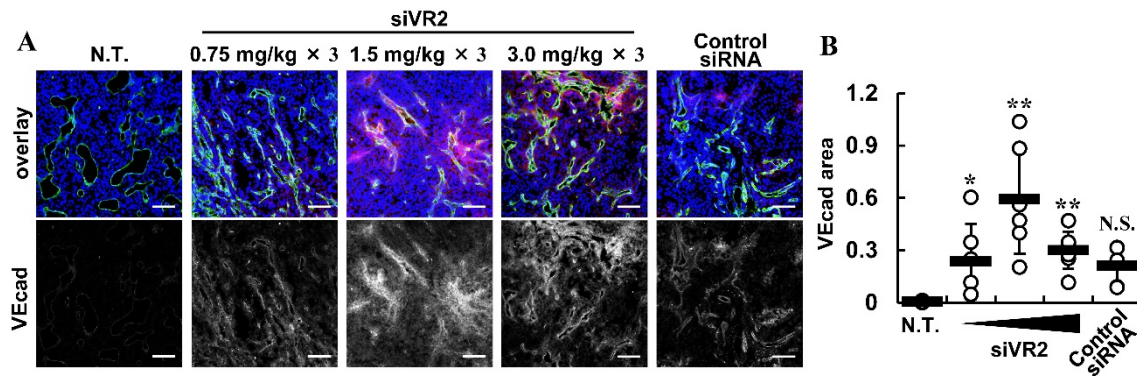
Figure 2. VEcad expression as an indicator of the integrity of the tumor vasculature. A) Representative images of VEcad expression. VEcad expression was investigated when siVR2 or control siRNA encapsulated in the RGD-MEND were 3 times administered at doses of 0.75, 1.5 or 3.0 mg/kg. In the upper panels, blue, green and red dots indicate the nucleus, CD31 and VEcad, respectively. In the lower panels, VEcad is shown in grayscale mode. B) Quantified data from A). VEcad pixels were normalized to nucleus pixels because theoretically VEcad didn't exist in vascular lumens. For statistical analysis, non repeated ANOVA was performed, followed by the Bonferroni test (vs. non treatment (N.T.)). P>0.05 was regarded as not statistically significant difference. Scale bars are 100 μm.
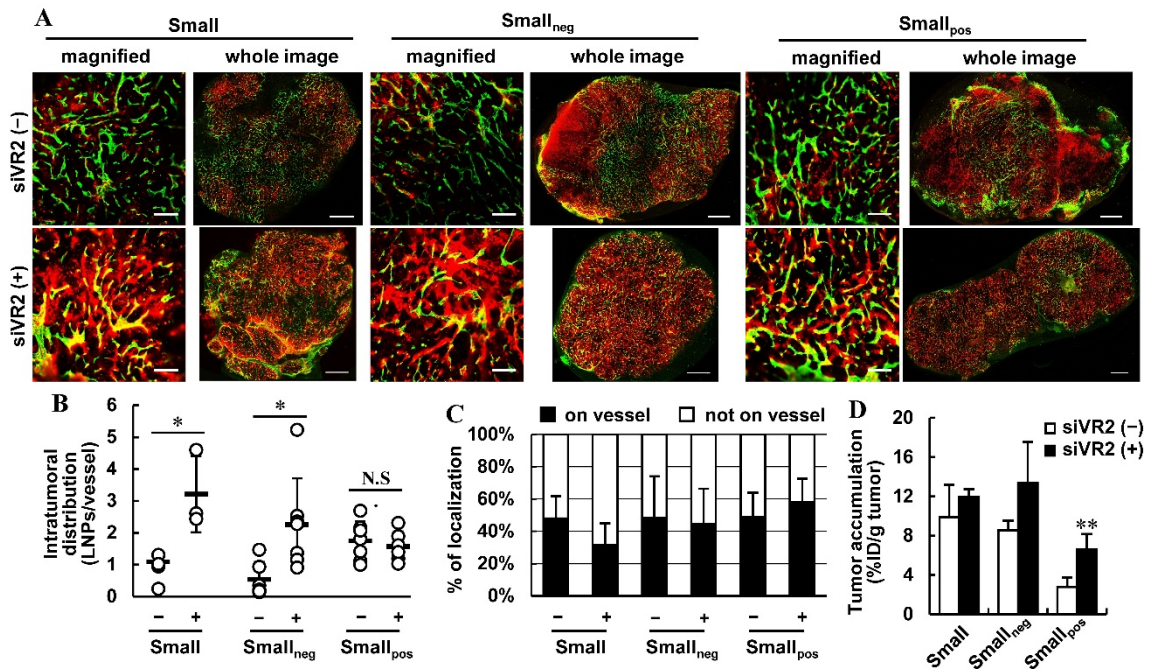
Figure 3. The intratumoral distribution and accumulation of neutral, negative and positive LPs. A) The effect of pre-siVR2 treatment on the intratumoral distribution of LPs. Green and red dots denote vessels and LPs, respectively. In this experiment, the dosage of each of the LPs was adjusted to shown the same AUC of fluorescence as the lowest $Small_{pos}$ LP. Scale bars are 100 μm for magnified images, 1000 μm for whole images. B) Quantitative data of the magnified images in Figure 2A. Red pixels indicating LPs were divided by green pixels indicating vessels. The signs – and + mean that siVR2 (–) and siVR2 (+), respectively. The Student's t-test was performed between siVR2 (−) and (+). *:p<0.05 (n=6-8). C) The change in localization of each LPs. White and black column mean LPs not on vessel and LPs co-localized on vessels, respectively. The signs – and + mean that siVR2 (–) and siVR2 (+), respectively. D) Accumulation amount of Small, $Small_{neg}$ and $Small_{pos}$ LPs with or without siVR2 treatment. Radioactivity in tumor tissues was measured by

liquid scintillation counting 24 h after OS-RC-2-bearing mice were administered with

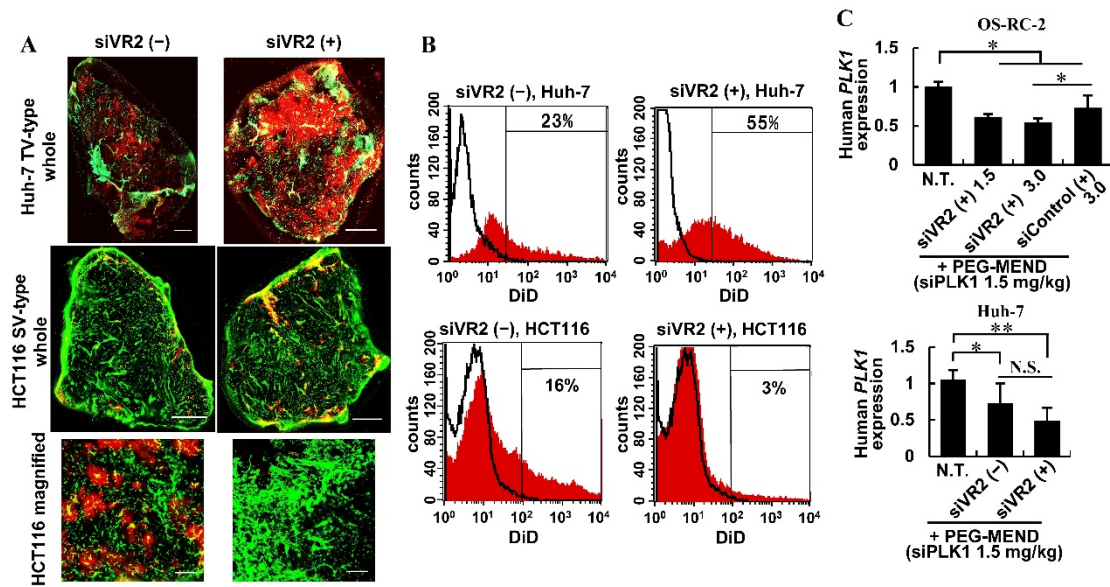[^{3}H]-CHE-labeled LPs. Data represent the mean ± standard deviation. (n=3)

Figure 4. The intratumoral distribution of LPs in comparison with tumor vessel (TV)-type and stroma vessel (SV)-type tumors. A) The effect of a pre-siVR2 treatment on the intratumoral distribution of LPs. Green and red dots means vessels and LPs, respectively. Scale bars are 100 μm for magnified images, 1000 μm for whole images. B) Quantitative data of LPs taken up by cancer cells. Black solid line means fluorescent intensity from un-treated mice. Red filled histogram means the fluorescent intensity from mice treated from fluorescent labeled LPs. The value indicates the population of cell fraction in which LPs-derived fluorescence was detected. C) Pharmacological effect of siVR2 on the silencing effect of tumor-targeting liposomal siRNA (PEG-MEND). Human *PLK1* mRNA expression was measured by qRT-PCR 24 h after the injection of PEG-MEND. siVR2 (+) 1.5 and siVR2 (+) mean that RGD-MEND loaded with siRNA against VEGFR2 was injected 3 times at a dose of 1.5 or 3.0 mg/kg, respectively, before the injection of the PEG-MEND. siControl (+) 3.0 means that siRNA against luciferase encapsulated in the RGD-MEND was administered 3

times at a dose of 3.0 mg/kg before the injection of the PEG-MEND. Upper and lower graphs means

the gene knockdown data in OS-RC-2 and Huh-7, respectively. Data represents mean ± standard

deviation. Statistical analyses were performed by non-repeated ANOVA, followed by SNK test.
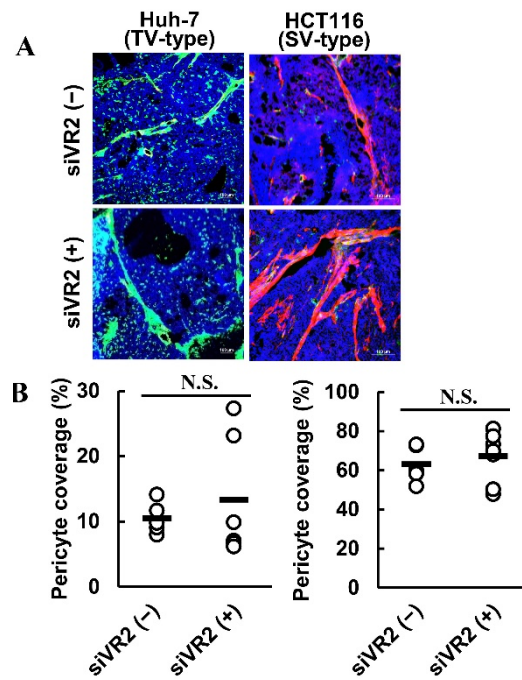
(n=3-6)

Figure 5. The change of COL1A1 expression by siVR2 treatment with tumor vessel (TV)-type and stroma vessel (SV)-type tumors. A) The effect of pre-siVR2 treatment on COL1A1 expression. Blue, green and red dots means nucleus, vessels and αSMA, respectively. Scale bars are 100 μm. B) Quantitative data of pericyte coverage. Statistical analysis was performed by Student's t-test. (n=5-6)
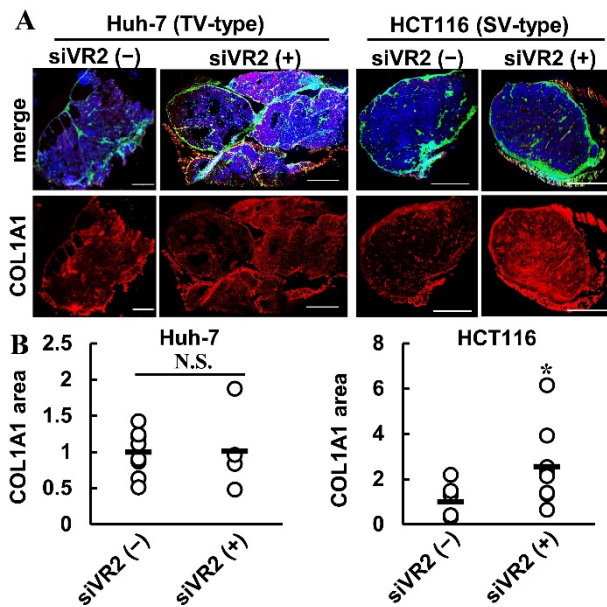
Figure 6. Alteration in type I collagen by siVR2 in comparison with tumor vessels (TV)-type and stroma vessels (SV)-type tumors. A) Whole images of COL1A1 in Huh-7 (TV-type) and HCT116 (SV-type) xenografts. COL1A1 in the tumor tissues with or without siVR2 pretreatment were observed. Blue, green and red dots indicate nucleus, vessels and COL1A1, respectively. Scale bars are 1000 μm.

References

[1] Y. Matsumura, H. Maeda, A new concept for macromolecular therapeutics in cancer chemotherapy: mechanism of tumoritropic accumulation of proteins and the antitumor agent smancs, Cancer Res, 46 (1986) 6387-6392.

[2] J.I. Hare, T. Lammers, M.B. Ashford, S. Puri, G. Storm, S.T. Barry, Challenges and strategies in anti-cancer nanomedicine development: An industry perspective, Adv Drug Deliv Rev, (2016).

[3] V. Riabov, A. Gudima, N. Wang, A. Mickley, A. Orekhov, J. Kzhyshkowska, Role of tumor associated macrophages in tumor angiogenesis and lymphangiogenesis, Front Physiol, 5 (2014) 75.

[4] K. Shiga, M. Hara, T. Nagasaki, T. Sato, H. Takahashi, H. Takeyama, Cancer-Associated Fibroblasts: Their Characteristics and Their Roles in Tumor Growth, Cancers (Basel), 7 (2015) 2443-2458.

[5] S. Taurin, H. Nehoff, K. Greish, Anticancer nanomedicine and tumor vascular permeability; Where is the missing link?, J Control Release, 164 (2012) 265-275.

[6] R. Bazak, M. Houri, S.E. Achy, W. Hussein, T. Refaat, Passive targeting of nanoparticles to cancer: A comprehensive review of the literature, Mol Clin Oncol, 2 (2014) 904-908.

[7] Y. Sakurai, T. Hada, S. Yamamoto, A. Kato, W. Mizumura, H. Harashima, A. Kato, W. Mizumura, H. Harashima, Remodeling of the extracellular matrix by endothelial cell-targeting siRNA improves the EPR-based delivery of 100 nm particles, Mol Ther, (2016).

[8] T.D. McKee, P. Grandi, W. Mok, G. Alexandrakis, N. Insin, J.P. Zimmer, M.G. Bawendi, Y. Boucher,

X.O. Breakefield, R.K. Jain, Degradation of fibrillar collagen in a human melanoma xenograft improves the efficacy of an oncolytic herpes simplex virus vector, Cancer Res, 66 (2006) 2509-2513.

[9] X. Zheng, B.A. Goins, I.L. Cameron, C. Santoyo, A. Bao, V.C. Frohlich, G.D. Fullerton, Ultrasound-guided intratumoral administration of collagenase-2 improved liposome drug accumulation in solid tumor xenografts, Cancer Chemother Pharmacol, 67 (2011) 173-182.

[10] B. Diop-Frimpong, V.P. Chauhan, S. Krane, Y. Boucher, R.K. Jain, Losartan inhibits collagen I synthesis and improves the distribution and efficacy of nanotherapeutics in tumors, Proc Natl Acad Sci U S A, 108 (2011) 2909-2914.

[11] K.A. Khan, R. Bicknell, Anti-angiogenic alternatives to VEGF blockade, Clin Exp Metastasis, 33 (2016) 197-210.

[12] K.J. Choi, I.H. Baik, S.K. Ye, Y.H. Lee, Molecular Targeted Therapy for Hepatocellular Carcinoma: Present Status and Future Directions, Biol Pharm Bull, 38 (2015) 986-991.

[13] F. Yuan, Y. Chen, M. Dellian, N. Safabakhsh, N. Ferrara, R.K. Jain, Time-dependent vascular regression and permeability changes in established human tumor xenografts induced by an anti-vascular endothelial growth factor/vascular permeability factor antibody, Proc Natl Acad Sci U S A, 93 (1996) 14765-14770.

[14] T. Nakahara, S.M. Norberg, D.R. Shalinsky, D.D. Hu-Lowe, D.M. McDonald, Effect of inhibition of vascular endothelial growth factor signaling on distribution of extravasated antibodies in tumors, Cancer

Res, 66 (2006) 1434-1445.

[15] H. Hurwitz, L. Fehrenbacher, W. Novotny, T. Cartwright, J. Hainsworth, W. Heim, J. Berlin, A. Baron, S. Griffing, E. Holmgren, N. Ferrara, G. Fyfe, B. Rogers, R. Ross, F. Kabbinavar, Bevacizumab plus irinotecan, fluorouracil, and leucovorin for metastatic colorectal cancer, N Engl J Med, 350 (2004) 2335-2342.

[16] S. Goel, A.H. Wong, R.K. Jain, Vascular normalization as a therapeutic strategy for malignant and nonmalignant disease, Cold Spring Harb Perspect Med, 2 (2012) a006486.

[17] T.D. Tailor, G. Hanna, P.S. Yarmolenko, M.R. Dreher, A.S. Betof, A.B. Nixon, I. Spasojevic, M.W. Dewhirst, Effect of pazopanib on tumor microenvironment and liposome delivery, Mol Cancer Ther, 9 (2010) 1798-1808.

[18] Y. Yoshizawa, K. Ogawara, A. Fushimi, S. Abe, K. Ishikawa, T. Araki, G. Molema, T. Kimura, K. Higaki, Deeper penetration into tumor tissues and enhanced in vivo antitumor activity of liposomal paclitaxel by pretreatment with angiogenesis inhibitor SU5416, Mol Pharm, 9 (2012) 3486-3494.

[19] V.P. Chauhan, T. Stylianopoulos, J.D. Martin, Z. Popovic, O. Chen, W.S. Kamoun, M.G. Bawendi, D. Fukumura, R.K. Jain, Normalization of tumour blood vessels improves the delivery of nanomedicines in a size-dependent manner, Nat Nanotechnol, 7 (2012) 383-388.

[20] N.R. Smith, D. Baker, M. Farren, A. Pommier, R. Swann, X. Wang, S. Mistry, K. McDaid, J. Kendrew, C. Womack, S.R. Wedge, S.T. Barry, Tumor stromal architecture can define the intrinsic tumor

response to VEGF-targeted therapy, Clin Cancer Res, 19 (2013) 6943-6956.

[21] Y. Sakurai, K. Kajimoto, H. Harashima, Anti-angiogenic nanotherapy via active targeting systems to tumors and adipose tissue vasculature, Biomater Sci, 3 (2015) 1253-1265.

[22] M. Hyodo, Y. Sakurai, H. Akita, H. Harashima, "Programmed packaging" for gene delivery, J Control Release, 193 (2014) 316-323.

[23] Y. Sakurai, K. Kajimoto, H. Hatakeyama, H. Harashima, Advances in an active and passive targeting to tumor and adipose tissues, Expert Opin Drug Deliv, 12 (2015) 41-52.

[24] Y. Sato, H. Hatakeyama, Y. Sakurai, M. Hyodo, H. Akita, H. Harashima, A pH-sensitive cationic lipid facilitates the delivery of liposomal siRNA and gene silencing activity in vitro and in vivo, J Control Release, 163 (2012) 267-276.

[25] Y. Hayashi, E. Suemitsu, K. Kajimoto, Y. Sato, A. Akhter, Y. Sakurai, H. Hatakeyama, M. Hyodo, N. Kaji, Y. Baba, H. Harashima, Hepatic Monoacylglycerol O-acyltransferase 1 as a Promising Therapeutic Target for Steatosis, Obesity, and Type 2 Diabetes, Mol Ther Nucleic Acids, 3 (2014) e154.

[26] S. Sato, K. Li, T. Kameyama, T. Hayashi, Y. Ishida, S. Murakami, T. Watanabe, S. Iijima, Y. Sakurai, K. Watashi, S. Tsutsumi, Y. Sato, H. Akita, T. Wakita, C.M. Rice, H. Harashima, M. Kohara, Y. Tanaka, A. Takaoka, The RNA sensor RIG-I dually functions as an innate sensor and direct antiviral factor for hepatitis B virus, Immunity, 42 (2015) 123-132.

[27] Y. Sato, Y. Note, M. Maeki, N. Kaji, Y. Baba, M. Tokeshi, H. Harashima, Elucidation of the

physicochemical properties and potency of siRNA-loaded small-sized lipid nanoparticles for siRNA delivery, J Control Release, 229 (2016) 48-57.

[28] K. Kajimoto, E. Suemitsu, Y. Sato, Y. Sakurai, H. Harashima, Liver-Specific Silencing of Lipin1 Reduces Fat Mass as Well as Hepatic Triglyceride Biosynthesis in Mice, Biol Pharm Bull, 39 (2016) 1653-1661.

[29] T. Watanabe, H. Hatakeyama, C. Matsuda-Yasui, Y. Sato, M. Sudoh, A. Takagi, Y. Hirata, T. Ohtsuki, M. Arai, K. Inoue, H. Harashima, M. Kohara, In vivo therapeutic potential of Dicer-hunting siRNAs targeting infectious hepatitis C virus, Sci Rep, 4 (2014) 4750.

[30] N. Yamamoto, Y. Sato, T. Munakata, M. Kakuni, C. Tateno, T. Sanada, Y. Hirata, S. Murakami, Y. Tanaka, K. Chayama, H. Hatakeyama, M. Hyodo, H. Harashima, M. Kohara, Novel pH-sensitive multifunctional envelope-type nanodevice for siRNA-based treatments for chronic HBV infection, J Hepatol, 64 (2016) 547-555.

[31] A. Akhter, Y. Hayashi, Y. Sakurai, N. Ohga, K. Hida, H. Harashima, A liposomal delivery system that targets liver endothelial cells based on a new peptide motif present in the ApoB-100 sequence, Int J Pharm, 456 (2013) 195-201.

[32] M. Tamaru, H. Akita, K. Kajimoto, Y. Sato, H. Hatakeyama, H. Harashima, An apolipoprotein E modified liposomal nanoparticle: ligand dependent efficiency as a siRNA delivery carrier for mouse-derived brain endothelial cells, Int J Pharm, 465 (2014) 77-82.

[33] H. Matsui, Y. Sato, H. Hatakeyama, H. Akita, H. Harashima, Size-dependent specific targeting and

efficient gene silencing in peritoneal macrophages using a pH-sensitive cationic liposomal siRNA carrier,

Int J Pharm, 495 (2015) 171-178.

[34] Y. Sakurai, H. Hatakeyama, Y. Sato, M. Hyodo, H. Akita, H. Harashima, Gene silencing via RNAi

and siRNA quantification in tumor tissue using MEND, a liposomal siRNA delivery system, Mol Ther, 21

(2013) 1195-1203.

[35] Y. Sakurai, H. Hatakeyama, H. Akita, H. Harashima, Improvement of doxorubicin efficacy using

liposomal anti-polo-like kinase 1 siRNA in human renal cell carcinomas, Mol Pharm, 11 (2014)

2713-2719.

[36] F. Danhier, A. Le Breton, V. Preat, RGD-based strategies to target alpha(v) beta(3) integrin in cancer

therapy and diagnosis, Mol Pharm, 9 (2012) 2961-2973.

[37] Y. Sakurai, H. Hatakeyama, Y. Sato, M. Hyodo, H. Akita, N. Ohga, K. Hida, H. Harashima,

RNAi-mediated gene knockdown and anti-angiogenic therapy of RCCs using a cyclic RGD-modified

liposomal-siRNA system, J Control Release, 173 (2014) 110-118.

[38] T. Hada, Y. Sakurai, H. Harashima, Optimization of a siRNA Carrier Modified with a pH-Sensitive

Cationic Lipid and a Cyclic RGD Peptide for Efficiently Targeting Tumor Endothelial Cells,

Pharmaceutics, 7 (2015) 320-333.

[39] Y. Sakurai, T. Hada, H. Harashima, Preparation of a Cyclic RGD: Modified Liposomal SiRNA

Formulation for Use in Active Targeting to Tumor and Tumor Endothelial Cells, Methods Mol Biol, 1364

(2016) 63-69.

[40] H. Maeda, J. Wu, T. Sawa, Y. Matsumura, K. Hori, Tumor vascular permeability and the EPR effect

in macromolecular therapeutics: a review, J Control Release, 65 (2000) 271-284.

[41] Y.L. Dorland, S. Huveneers, Cell-cell junctional mechanotransduction in endothelial remodeling,

Cell Mol Life Sci, (2016).

[42] Y. Zhang, L. Zhang, Y. Li, S. Sun, H. Tan, Different contributions of clathrin- and caveolae-mediated

endocytosis of vascular endothelial cadherin to lipopolysaccharide-induced vascular hyperpermeability,

PLoS One, 9 (2014) e106328.

[43] F. Wessel, M. Winderlich, M. Holm, M. Frye, R. Rivera-Galdos, M. Vockel, R. Linnepe, U. Ipe, A.

Stadtmann, A. Zarbock, A.F. Nottebaum, D. Vestweber, Leukocyte extravasation and vascular

permeability are each controlled in vivo by different tyrosine residues of VE-cadherin, Nat Immunol, 15

(2014) 223-230.

[44] M.G. Vander Heiden, L.C. Cantley, C.B. Thompson, Understanding the Warburg effect: the

metabolic requirements of cell proliferation, Science, 324 (2009) 1029-1033.

[45] W. Yeeprae, S. Kawakami, S. Suzuki, F. Yamashita, M. Hashida, Physicochemical and

pharmacokinetic characteristics of cationic liposomes, Pharmazie, 61 (2006) 102-105.

[46] V.P. Chauhan, J.D. Martin, H. Liu, D.A. Lacorre, S.R. Jain, S.V. Kozin, T. Stylianopoulos, A.S.

Mousa, X. Han, P. Adstamongkonkul, Z. Popovic, P. Huang, M.G. Bawendi, Y. Boucher, R.K. Jain, Angiotensin inhibition enhances drug delivery and potentiates chemotherapy by decompressing tumour blood vessels, Nat Commun, 4 (2013) 2516.

[47] G. Ishii, A. Ochiai, S. Neri, Phenotypic and functional heterogeneity of cancer-associated fibroblast within the tumor microenvironment, Adv Drug Deliv Rev, 99 (2016) 186-196.

[48] A.C. Dudley, Tumor endothelial cells, Cold Spring Harb Perspect Med, 2 (2012) a006536.

[49] H. Hashizume, P. Baluk, S. Morikawa, J.W. McLean, G. Thurston, S. Roberge, R.K. Jain, D.M. McDonald, Openings between defective endothelial cells explain tumor vessel leakiness, Am J Pathol, 156 (2000) 1363-1380.

[50] B. Haley, E. Frenkel, Nanoparticles for drug delivery in cancer treatment, Urol Oncol, 26 (2008) 57-64.

[51] W.W. Ma, M. Hidalgo, The winning formulation: the development of paclitaxel in pancreatic cancer, Clin Cancer Res, 19 (2013) 5572-5579.

[52] J.E. Schnitzer, gp60 is an albumin-binding glycoprotein expressed by continuous endothelium involved in albumin transcytosis, Am J Physiol, 262 (1992) H246-254.

[53] R.D. Minshall, C. Tiruppathi, S.M. Vogel, W.D. Niles, A. Gilchrist, H.E. Hamm, A.B. Malik, Endothelial cell-surface gp60 activates vesicle formation and trafficking via G(i)-coupled Src kinase signaling pathway, J Cell Biol, 150 (2000) 1057-1070.

[54] S.M. Vogel, R.D. Minshall, M. Pilipovic, C. Tiruppathi, A.B. Malik, Albumin uptake and transcytosis in endothelial cells in vivo induced by albumin-binding protein, Am J Physiol Lung Cell Mol Physiol, 281 (2001) L1512-1522.

[55] H. Suzuki, Y.H. Bae, Evaluation of drug penetration with cationic micelles and their penetration mechanism using an in vitro tumor model, Biomaterials, 98 (2016) 120-130.

[56] M. Simons, E. Gordon, L. Claesson-Welsh, Mechanisms and regulation of endothelial VEGF receptor signalling, Nat Rev Mol Cell Biol, 17 (2016) 611-625.

[57] N.N. Rahbari, D. Kedrin, J. Incio, H. Liu, W.W. Ho, H.T. Nia, C.M. Edrich, K. Jung, J. Daubriac, I. Chen, T. Heishi, J.D. Martin, Y. Huang, N. Maimon, C. Reissfelder, J. Weitz, Y. Boucher, J.W. Clark, A.J. Grodzinsky, D.G. Duda, R.K. Jain, D. Fukumura, Anti-VEGF therapy induces ECM remodeling and mechanical barriers to therapy in colorectal cancer liver metastases, Sci Transl Med, 8 (2016) 360ra135.

[58] A. Meyer, J. Auernheimer, A. Modlinger, H. Kessler, Targeting RGD recognizing integrins: drug development, biomaterial research, tumor imaging and targeting, Curr Pharm Des, 12 (2006) 2723-2747.

[59] M.R. Kano, Y. Bae, C. Iwata, Y. Morishita, M. Yashiro, M. Oka, T. Fujii, A. Komuro, K. Kiyono, M. Kaminishi, K. Hirakawa, Y. Ouchi, N. Nishiyama, K. Kataoka, K. Miyazono, Improvement of cancer-targeting therapy, using nanocarriers for intractable solid tumors by inhibition of TGF-beta signaling, Proc Natl Acad Sci U S A, 104 (2007) 3460-3465.

[60] H. Cabral, Y. Matsumoto, K. Mizuno, Q. Chen, M. Murakami, M. Kimura, Y. Terada, M.R. Kano, K.

Miyazono, M. Uesaka, N. Nishiyama, K. Kataoka, Accumulation of sub-100 nm polymeric micelles in poorly permeable tumours depends on size, Nat Nanotechnol, 6 (2011) 815-823.

[61] S. Chen, Y.Y. Tam, P.J. Lin, M.M. Sung, Y.K. Tam, P.R. Cullis, Influence of particle size on the in vivo potency of lipid nanoparticle formulations of siRNA, J Control Release, 235 (2016) 236-244.

[62] G.H. Petersen, S.K. Alzghari, W. Chee, S.S. Sankari, N.M. La-Beck, Meta-analysis of clinical and preclinical studies comparing the anticancer efficacy of liposomal versus conventional non-liposomal doxorubicin, J Control Release, 232 (2016) 255-264.

[63] L. Miao, J.M. Newby, C.M. Lin, L. Zhang, F. Xu, W.Y. Kim, M.G. Forest, S.K. Lai, M.I. Milowsky, S.E. Wobker, L. Huang, The Binding Site Barrier Elicited by Tumor-Associated Fibroblasts Interferes Disposition of Nanoparticles in Stroma-Vessel Type Tumors, ACS Nano, (2016).

[64] D. Keskin, J. Kim, V.G. Cooke, C.C. Wu, H. Sugimoto, C. Gu, M. De Palma, R. Kalluri, V.S. LeBleu, Targeting vascular pericytes in hypoxic tumors increases lung metastasis via angiopoietin-2, Cell Rep, 10 (2015) 1066-1081.